processes

MDPI

Article

Scheduling Control Considering Model Inconsistency of Membrane-Wing Aircraft

Yanxuan Wu *, Yifan Fu, Zhengjie Wang, Yang Yu and Hao Li

School of Mechatronics Engineering, Beijing Institute of Technology, Beijing 100081, China; alice020328@163.com (Y.F.); wangzhengjie@bit.edu.cn (Z.W.); yangyu.bit2012@gmail.com (Y.Y.); lihao0633@126.com (H.L.)
* Correspondence: alexwyx@bit.edu.cn

Abstract

Inconsistency in the structural strengths of a membrane wing under positive and negative loads has undesirable impacts on the aeroelastic deflections of the wing, which results in more significant flight control system modeling errors and worsens the performance of the aircraft. In this paper, an integrated dynamic model is derived for a membrane-wing aircraft based on the structural dynamics equation of the membrane wing and the flight dynamics equation of the traditional fixed wing. Based on state feedback control theory, an autopilot system is designed to unify the flight and control properties of different flight and wing deformation statuses. The system uses models of different operating regions to estimate the dynamic response of the vehicle and compares the estimation results with the sensor signals. Based on the compared results, the autopilot can identify the overall flight and select the correct operating region for the control system. By switching to the operating region with the minimum modeling error, the autopilot system maintains good flight performance while flying in turbulence. According to the simulation results, compared with traditional rigid aircraft autopilots, the proposed autopilot can reduce the absolute maximum attack angles by nearly 27% and the absolute maximum wingtip twist angles by nearly 25% under gust conditions. This enhanced robustness and stability performance demonstrates the autopilot's significant potential for practical deployment in micro-aerial vehicles, particularly in applications demanding reliable operation under turbulent conditions, such as military surveillance, environmental monitoring, precision agriculture, or infrastructure inspection.

Keywords: flight dynamics; aeroelasticity; state observer; gust suppression; state feedback control

check for updates

Academic Editors: Weicun Zhang and Quanmin Zhu

Received: 30 June 2025
Revised: 22 July 2025
Accepted: 23 July 2025
Published: 25 July 2025

Citation: Wu, Y.; Fu, Y.; Wang, Z.; Yu, Y.; Li, H. Scheduling Control Considering Model Inconsistency of Membrane-Wing Aircraft. *Processes* **2025**, *13*, 2367. https://doi.org/10.3390/pr13082367

Correction Statement: This article has been republished with a minor change. The change does not affect the scientific content of the article and further details are available within the backmatter of the website version of this article.

Copyright: © 2025 by the authors. Licensee MDPI, Basel, Switzerland. This article is an open access article distributed under the terms and conditions of the Creative Commons Attribution (CC BY) license (https://creativecommons.org/licenses/by/4.0/).

1. Introduction

The bio-inspired membrane wing technology has emerged as a pivotal innovation in micro-air vehicle (MAV) design owing to its unique aeroelastic properties that enable deformation through fluid–structure interactions [1–3]. Derived from bat flight mechanics, these compliant structures demonstrate passive flow condition adaptability—a critical advantage in the low-Reynolds-number regimes that are characteristic of MAV operations. The aviation field defines the range of $10^4 \sim 10^5$ as the low-Reynolds-number range [4]. Conventional aircrafts generally have a flight Reynolds number in the range of 10^6, while MAVs typically have flight Reynolds number in the range of $10^4 \sim 10^5$ due to small geometric scales and low flight velocities. Therefore, MAVs are in the low-Reynolds-number range of aerodynamic environments, which can induce complex phenomena,

including laminar separation and boundary layer transition [5], necessitating high-attack-angle configurations that increase adaptability to aerodynamic stall when encountering gusts [6].

The current biological mitigation strategies can be divided into two approaches: active flapping wing systems and passive morphing wing solutions [1]. While flapping mechanisms inspired by ornithopters exhibit exceptional maneuverability, their practical implementation is constrained by their excessive energy consumption and mechanical complexity. In contrast, morphing wings like membrane wings have gained prominence as an energy-efficient alternative, achieving flow control through passive camber modulation with minimal weight penalties [7,8]. In addition, membrane wings can be folded around the fuselage for storage and transportation [9,10]. These inherent advantages have promoted the development of membrane-wing aerial vehicles (MWAVs) [11]. The University of Florida's work demonstrates enhanced gust resistance through adaptive washout mechanisms [12–14]. Subsequent studies have further validated their stall delay capabilities and disturbance attenuation through strategic membrane deflection [15,16]. Active membrane wing control has made significant progress in recent years. Wang et al. synchronously measured flexible membrane wings and their impact on aerodynamic force. Based on their results, they proposed an adaptive control method applying deformation and vibration excitation with specific frequencies [17]. Feng et al. proposed active deformation, achieved with macrofiber composite (MFC) actuators which are attached to the upper surface of the wings [18]. The concept of a variable wingspan wing grid (WGM), achieved by mimicking the flight mechanism of ornithopters, was proposed recently [19]. Negahban et al. proposed a twist morphing aileron and winglet design to improve the rolling efficiency and reduce induced drag [20]. Other ways to help pilot MWAVs include having large control surfaces and a suitable autopilot system [21–23].

In order to meet the control requirements of MWAVs described above, a controller design is needed, with a focus on state estimation and feedback. Currently, there is a lack of reported work specifically dedicated to the development of state observers and state feedback control schemes tailored for MWAVs. However, we can learn from various control strategies that are applicable to complex aerospace systems. The Active Disturbance Rejection Control (ADRC) theory can be used for controlling a single objective [24]. ADRC consists of three main parts: a tracking differentiator (TD), nonlinear state feedback controller, and extended observer (ESO). On this basis, Guo et al. conducted in-depth research on the convergence of the ADRC method [25]. Currently, ADRC and ESO have been applied in the aerospace industry. Optimal control is required for controlling multiple objectives, including the classical variational method, dynamic programming, and the minimum principle [26]. In addition, sliding mode control (SMC) has also been successfully applied in fields such as aircraft flight control, active aeroelastic control, and active control of structural vibration. Erfan Rezaei et al. studied a fixed-time observer-based adaptive non-singular sliding mode approach for a flexible spacecraft subject to vibrations of flexible modes, unknown bounded disturbance, and inherent uncertainty [27].

Despite these advances, critical challenges persist in MWAV implementation. Although membrane wings share dynamic similarities with conventional fixed-wing aircrafts in control responsiveness and structural weight [28–30], their aeroelastic behavior introduces unique operational complexities. Comparative analyses reveal significant aerodynamic performance deviations from their rigid-wing counterparts under equivalent configurations [31–33], exacerbated by asymmetric stiffness responses to positive versus negative aerodynamic loads [34]. More critically, the inherent flexibility of membrane wings presents a double-edged sword: under extreme negative overload conditions, it may induce catastrophic buckling deformations. This specific failure mode, arising directly from

the material compliance that is essential for the wing's function, poses a severe threat to structural integrity and flight safety, particularly during aggressive maneuvers or severe gust encounters. Consequently, the phenomena outlined above—especially the critical buckling risk under negative loads—underscore the urgent need for a comprehensive characterization of membrane wings' aeroelasticity. Such characterization is essential not only to understand performance deviations under normal conditions but crucially to predict and mitigate catastrophic failure modes across the diverse flight regimes encountered by MWAVs.

In this article, a simple autopilot system which can cope with the model inconsistency caused by asymmetric stiffness under positive loads and negative loads is proposed. The aeroelastic impacts on flight dynamics due to membrane wings are investigated, and a simplified dynamic model is derived in Section 2. In addition, the state feedback control system and corresponding controller scheduling mechanism are also designed based on the estimation errors of the state observers in Section 2. The estimation performances from state observers are studied and compared by setting different flight conditions in Section 3. Furthermore, the performance of the autopilot systems is demonstrated in the presence of discrete gusts in Section 3. Sections 4 and 5 offer a discussion and conclusion regarding the research findings.

2. Materials and Methods

Being foldable is one of the main features of MWAVs. The wing is specifically designed to be thin and curved in a chord-wise direction, as illustrated in Figure 1. The material of the wing is carbon fiber made by Suzhou Noen Composite Materials Co., Ltd, China. The leading edge is designed in a half arc shape to enhance its structural strength, while the trailing edge is designed to be weak on purpose to be used as ailerons. As a result, the main elastic axis is located very close to the leading edge, and the membrane wing tends to have negative aerodynamic force under positive aerodynamic loads, and vice versa, as shown in Figure 1. This feature gives MWAVs the capability of passive gust alleviation, as well as the ability to fly at a high attack angle.

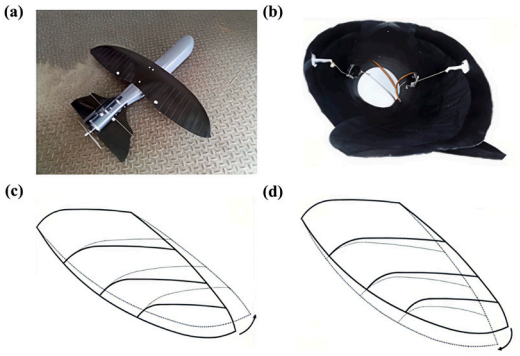


Figure 1. Demonstration of an MWAV. (**a**) The overall configuration. (**b**) The folded membrane wing. (**c**) Wing deflection under positive loads. (**d**) Wing deflection under negative loads.

The membrane wing lacks a wing-box structure. Instead, the curved leading edge offers an alternative load-carrying structure like a U-beam. This kind of structure tends to have different deformation amplitudes under different loads, usually causing obviously different structural strength properties in opposite directions. This is a major threat to the safety and reliability of operation. Figure 2 shows the testing equipment, the testing wing, and how to apply force for the ground test.

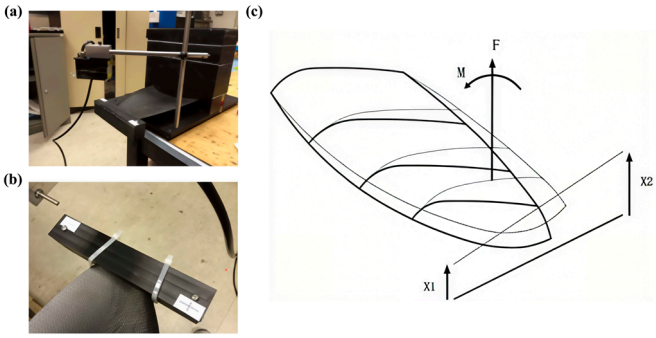


Figure 2. Ground test for structural strength properties. (**a**) The testing equipment. (**b**) The testing wing. (**c**) The method of applying force. (F represents the applied force, M represents the applied torque, x_1 represents the deformation displacement of the leading edge, x_2 represents the deformation displacement of the trailing edge).

Table 1 demonstrates the structural strength properties of the testing membrane wing under different load conditions.

Table 1. Structural strength properties under different load conditions.

	Section 1	**Section 2**	**Section 3**	**Section 4**	**Section 5**
Positive loads			Concentrated force on wingtip, lower than 20.6 N		
E [1] (Pa)	9.853×10^8	3.273×10^8	1.523×10^8	7.603×10^7	5.053×10^7
G [2] (Pa)	3.883×10^6	2.653×10^6	1.473×10^6	1.503×10^6	2.663×10^6
Negative loads			Concentrated force on wingtip, lower than 6.2 N		
E (Pa)	6.073×10^8	1.713×10^8	7.913×10^7	6.283×10^7	4.443×10^7
G (Pa)	2.513×10^6	1.223×10^6	8.613×10^5	1.163×10^6	1.863×10^6

[1] E represents the elastic modulus. [2] G represents the shear modulus of elasticity.

Table 1 demonstrates significantly lower structural strength under negative loads compared to positive loads. This is evidenced by lower elastic and shear moduli under negative loads, despite the smaller concentrated force that is applied to the wingtip.

To design an autopilot which is capable of regulating the aerodynamic loads in an appropriate regime, there are two major steps:

1. A couple of simple integrated control models need to be derived from a flight dynamics model and structural dynamics model under different aerodynamic loads. Due to the different structural strength characteristics of membrane wings under positive and negative loads, two sets of control models are designed.
2. The controller needs to be able to compensate for the aeroelastic effects of membrane wings, and the mechanics should be designed to keep the autopilot in the correct operating region based on the current flight conditions.

2.1. Integrated Dynamic Model

A structural dynamics equation of a membrane wing can be constructed as follows:

$$M\ddot{x}_E + D_S\dot{x}_E + Kx_E = P_Q(x_R, x_E) + P_U(\dot{x}_E) + P_I(\dot{x}_R) + P_G(x_R) \quad (1)$$

This fundamental equation governs the dynamic deformation response of the membrane wing under various forces. In Equation (1), x_R represents the state of rigid body motion, x_E represents the structural deformation displacement of the membrane wing, M represents the mass matrix of the membrane wing, D_S represents the structural damping matrix of the membrane wing, and K represents the stiffness matrix of the membrane wing.

The left side of the equation represents the structural response, that is, how the wing resists motion. Specifically, $M\ddot{x}_E$ represents the inertial force resisting acceleration, $D_S\dot{x}_E$ represents the structural damping force which dissipates energy, and Kx_E represents the elastic restoring force generated by the wing's stiffness as it deforms away from its equilibrium shape. Meanwhile, the right side of the equation represents the external force, that is, what factors drive the motion of the wing. Specifically, $P_Q(x_R, x_E)$ represents the quasisteady aerodynamic force, $P_U(\dot{x}_E)$ represents the unsteady aerodynamic force, $P_I(\dot{x}_R)$ represents the inertial force load due to rigid body acceleration, and $P_G(x_R)$ represents gravity.

Assumption 1: Quasisteady aerodynamic force assumption [35]. The carbon fiber thin-film membrane wing has the characteristics of light weight and small scale, and the inertial coupling effect caused by structural deformation is weak. In addition, the membrane-wing aircraft has a lower flight speed, smaller wing structure deformations, and a lower proportion of unsteady aerodynamic forces. In equilibrium, gravity is usually balanced by the static elastic restoring force of the structure. Small perturbation analysis focuses on dynamic increments, where the change in gravity is a high-order small amount relative to the elastic restoring force, so the dynamic part of the gravity term can be ignored. Therefore, for membrane-wing aircrafts, the aerodynamic coupling relationship P_Q plays a major role in the rigid flexible coupling dynamics relationship.

The quasisteady aerodynamic force $P_Q(x_R, x_E)$ in Equation (1) can be expressed as follows:

$$P_Q(x_R, x_E) = K_{AE}x_E + A_{RM}x_R \tag{2}$$

where K_{AE} represents the aerodynamic stiffness matrix of membrane wing, and A_{RM} represents the aerodynamic calculation matrix for rigid body motion.

Based on the small perturbation principle [36], we can obtain Equation (3) by substituting Equation (2) into Equation (1):

$$\begin{pmatrix} \Delta\dot{x}_E \\ \Delta\ddot{x}_E \end{pmatrix} = \begin{pmatrix} 0 & I \\ -M^{-1}(K - K_{AE}) & -M^{-1}D_S \end{pmatrix} \begin{pmatrix} \Delta x_E \\ \Delta\dot{x}_E \end{pmatrix} + \begin{pmatrix} 0 \\ M^{-1}A_{RM} \end{pmatrix} \Delta x_R \tag{3}$$

In Equation (3), we can define the system matrix of elastic body motion A_{EE} and the pneumatic coupling matrix A_{ER} as follows:

$$A_{EE} = \begin{pmatrix} 0 & I \\ -M^{-1}(K - K_{AE}) & -M^{-1}D_S \end{pmatrix} = \begin{pmatrix} 0 & I \\ A_{EE-21} & A_{EE-22} \end{pmatrix} \tag{4}$$

$$A_{ER} = \begin{pmatrix} 0 \\ M^{-1}A_{RM} \end{pmatrix} = \begin{pmatrix} 0 \\ A_{ER-2} \end{pmatrix} \tag{5}$$

The flight dynamics equation of a membrane-wing aircraft can be simplified to the particle dynamics equation of a rigid fuselage, as shown in Equation (6) [37]:

$$\begin{cases} m\dot{u} + m(qw - rv) = X \\ m\dot{v} + m(ru - pw) = Y \\ m\dot{w} + m(pv - qu) = Z \\ I_x\dot{p} - I_{xz}\dot{r} + qr(I_z - I_y) - I_{xz}pq = L \\ I_y\dot{q} + rq(I_x - I_z) + I_{xz}(p^2 - q^2) = M \\ -I_{xz}\dot{p} + I_z\dot{r} + pq(I_y - I_x) + I_{xz}qr = N \end{cases} \tag{6}$$

This equation describes the complete 6-DOF rigid body motion of the fixed-wing aircraft in the body-fixed coordinate frame. It consists of three force equations and three moment equations. In Equation (6), m represents the aircraft mass; u, v, and w represent the

linear velocity in the body along the x, y, and z axes; p, q, and r represent angular velocity components about the body's x, y, and z axes; I_x, I_y, and I_z represent moments of inertia about the body's x, y, and z axes; I_{xz} is the product of inertia in the x-z plane; X, Y, and Z represent net external force components in the body axes; and L, M, and N represent net external moment components about the body axes. Figure 3 depicts the above-described physical quantities in the body-fixed coordinate frame. The left side of each equation represents the rate of change in linear momentum or angular momentum of the aircraft as seen in the rotating body frame. This includes both the direct acceleration and coupling terms arising because the body frame is rotating. The right side of each equation represents the net external forces and moments applied to the aircraft.

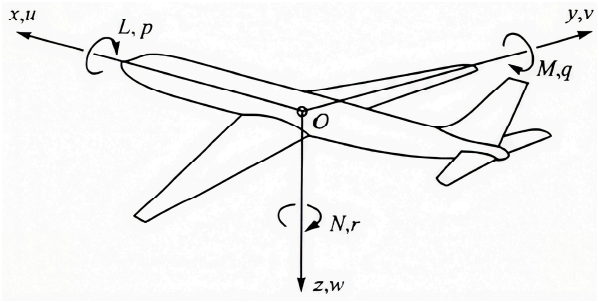


Figure 3. The physical measurements in the body-fixed coordinate frame.

We use $M_{CG}(\dot{x}_R) + f_{CG}(x_R)$ to substitute the left side of Equation (6), so that the flight dynamics equation of a membrane-wing aircraft can be rephrased as follows:

$$M_{CG}(\dot{x}_R) + f_{CG}(x_R) = F_W(x_R, x_E, \dot{x}_E, \ddot{x}_E) + F_B(x_R) + F_T(x_R) + F_G(x_R) \tag{7}$$

where F_W represents the force transmitted from the membrane wing to the rigid fuselage structure through the wing root, F_B represents aerodynamics of the fuselage and tail wing, F_T represents thrust, and F_G represents gravity.

The finite element model of a membrane wing structure is a beam model arranged along the elastic axis of the wing. Assuming that the membrane wing is defined as a three-node two-beam element structure like shown in Figure 4, F_W can be expressed described below [38].

$$F_w = \begin{pmatrix} 1 & 0 & 0 & 1 & 0 & 0 \\ -1.4c & 0 & 1 & -1.8c & 0 & 1 \end{pmatrix} (P_Q + F_I) = R_1(P_Q + F_I) \tag{8}$$

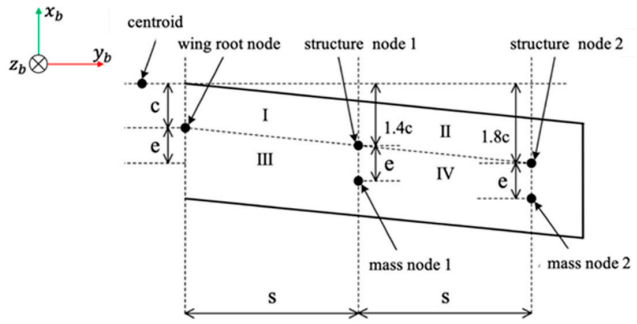


Figure 4. The finite element model of a flexible wing structure. (c, $1.4c$, $1.8c$ represent the distance between each structure node and the centroid on the O_bx_b axis of the body coordinate system, e represents the distance between each structure node and mass node on the O_bx_b axis of the body coordinate system, s represents the distance between each structure node and wing root node on the O_by_b axis of the body coordinate system).

In Equation (8), F_I represents the inertial force distribution load vector and can be expressed as follows:

$$F_I = -M\ddot{x}_E \tag{9}$$

The mass matrix of the longitudinal rigid body motion of membrane-wing aircraft M_R can be expressed as follows:

$$M_R = \begin{pmatrix} m & 0 \\ 0 & I_y \end{pmatrix} \tag{10}$$

where m represents the total weight of the aircraft, and I_y represents the moment of inertia of the aircraft on the $O_b y_b$ axis of the body coordinate system.

To capture the coupling effect of elastic body motion on rigid body motion, we only retain F_W, which uniquely contains elastic deformation on the right side of Equation (7). After substituting Equations (2) and (9) into Equation (8) and subsequently substituting Equation (8) into Equation (7), we apply the small perturbation principle. By defining the state vector as $\Delta\dot{x}_R = \left(\Delta\dot{\alpha}, \Delta\dot{q}\right)$, the resulting expression takes the form of Equation (11):

$$\begin{pmatrix} \Delta\dot{\alpha} \\ \Delta\dot{q} \end{pmatrix} = \begin{pmatrix} {u_0}^{-1} & 0 \\ 0 & 1 \end{pmatrix} {M_R}^{-1} R_1 K_{AE} \Delta x_E = A_{RE-1} \Delta x_E \tag{11}$$

According to Equation (11), we can define the pneumatic coupling matrix A_{RE} as follows:

$$A_{RE} = \begin{pmatrix} A_{RE-1} & 0 \end{pmatrix} \tag{12}$$

A linearized dynamic model for a membrane-wing aircraft under the condition of considering only quasisteady aerodynamic coupling relationships is established as follows [39–41]:

$$\begin{pmatrix} \Delta\dot{x}_R \\ \Delta\dot{x}_{EE} \end{pmatrix} = \begin{pmatrix} A_{RR} & A_{RE} \\ A_{ER} & A_{EE} \end{pmatrix} \begin{pmatrix} \Delta x_R \\ \Delta x_{EE} \end{pmatrix} + B\Delta u \tag{13}$$

In Equation (13), A_{RR} represents the system matrix of rigid body motion and can be expressed as follows [36]:

$$A_{RR} = \begin{pmatrix} \frac{Z_\alpha}{u_0} & 1 \\ M_\alpha + M_{\dot{\alpha}} \frac{Z_\alpha}{u_0} & M_q + M_{\dot{\alpha}} \end{pmatrix} \tag{14}$$

In Equation (13), Δx_{EE} represents the set of structural deformation displacements of membrane wings and its derivatives:

$$\Delta x_{EE} = \left(\Delta x_E, \Delta\dot{x}_E\right)^T \tag{15}$$

If we expand the Δx_{EE} term in Equation (13), it can be rephrased as follows:

$$\begin{pmatrix} \Delta\dot{x}_R \\ \Delta\dot{x}_E \\ \Delta\ddot{x}_E \end{pmatrix} = \begin{pmatrix} A_{RR} & A_{RE-1} & 0 \\ 0 & 0 & I \\ A_{ER-2} & A_{EE-21} & A_{EE-22} \end{pmatrix} \begin{pmatrix} \Delta x_R \\ \Delta x_E \\ \Delta\dot{x}_E \end{pmatrix} + \begin{pmatrix} B_R \\ 0 \\ B_E \end{pmatrix} \Delta u \tag{16}$$

Deformation of a membrane wing structure (Δx_E) can be divided into two parts, instantaneous equilibrium deformation of a membrane wing structure (Δx_{EB}) and residual deformation of a membrane wing structure ($\Delta\widetilde{x}_E$), as follows:

$$\Delta x_E = \Delta x_{EB} + \Delta\widetilde{x}_E \tag{17}$$

The definition of instantaneous equilibrium deformation Δx_{EB} is assuming that the membrane wing structure has no inertia and there is no transitional process in the dynamic response of structural deformation. Under such assumptions, the membrane wing structure always satisfies the condition of static equilibrium with external loads; that is, $\Delta\dot{x}_{EB} = \Delta\ddot{x}_{EB} = 0$. According to Equation (16), Δx_{EB}, Δx_R, and Δu should satisfy the static equilibrium condition as follows:

$$\begin{pmatrix} 0 & I \\ A_{EE-21} & A_{EE-22} \end{pmatrix} \begin{pmatrix} \Delta x_{EB} \\ \Delta \dot{x}_{EB} \end{pmatrix} + \begin{pmatrix} 0 \\ M^{-1} A_{RM} \end{pmatrix} \Delta x_R + B_E \Delta u = 0 \tag{18}$$

Δx_{EB} can be derived from Equation (18) as follows:

$$\Delta x_{EB} = -{A_{EE-21}}^{-1} A_{ER-2} \Delta x_R - {A_{EE-21}}^{-1} B_E \Delta u \tag{19}$$

Table 2 demonstrates the model frequency of short-period motion and membrane wing structure.

Table 2. Model frequency of short-period motion and membrane wing structure.

Dynamic Properties	Positive Load Conditions	Negative Load Conditions
Short-period motion	f = 2.77	f = 2.66
Model frequencies of membrane wing structure	f_1 = 22.40	f_1 = 14.38
	f_2 = 59.54	f_2 = 35.49
	f_3 = 94.15	f_3 = 55.59
	f_4 = 118.68	f_4 = 67.94

Assumption 2: Frequency separation assumption [35]. Because of the small scale of membrane wings and the unnoticeable inertial coupling effects due to the extremely light-weight structure, the model frequency of composite thin-film membrane wings is significantly higher than the short-period motion frequency of the aircraft. Therefore, the rigid body motion state variable Δx_R, which reflects changes in the flight state of the aircraft, belongs to a slow time-varying state variable, and the corresponding instantaneous equilibrium deformation Δx_{EB} is also a slow time-varying state variable. The elastic body motion state variable Δx_E reflecting the deformation motion of the membrane wing structure belongs to the fast time-varying state variable, and the corresponding residual deformation $\Delta \widetilde{x}_E$ is also a fast time-varying variable.

Replace Δx_E with $\Delta \widetilde{x}_E$, and substitute Δx_{EB} obtained in Equation (19) into the linearized dynamic model in Equation (16); then we can obtain a new linearized dynamic model as follows [42]:

$$\begin{pmatrix} \Delta \dot{x}_R \\ \Delta \dot{\widetilde{x}}_E \\ \Delta \ddot{\widetilde{x}}_E \end{pmatrix} = \begin{pmatrix} A^*_{RR} & A_{RE-1} & 0 \\ 0 & 0 & I \\ A_{ER-2} & A_{EE-21} & A_{EE-22} \end{pmatrix} \begin{pmatrix} \Delta x_R \\ \Delta \widetilde{x}_E \\ \Delta \dot{\widetilde{x}}_E \end{pmatrix} + \begin{pmatrix} B^*_R \\ 0 \\ B_E \end{pmatrix} \Delta u + \begin{pmatrix} 0 \\ E^* \end{pmatrix} \Delta w \tag{20}$$

where $\begin{pmatrix} 0 \\ E^* \end{pmatrix} \Delta w$ represents higher-order derivative terms containing rigid body motion and control inputs. ${A_{RR}}^*$ and ${B_R}^*$ contain aerodynamic coupling effects and can be expressed as follows:

$$A^*_{RR} = A_{RR} - A_{RE-1} A^{-1}_{EE-21} A_{ER-2} \tag{21}$$

$$B^*_R = B_R - A_{RE-1} A^{-1}_{EE-21} B_E \tag{22}$$

We can ignore fast time-varying variables under the condition that the flight speed of the membrane-wing aircraft is significantly different to the flutter speed. Therefore, the dynamic models that we are concerned about can be expressed as follows based on Equation (20):

$$\Delta \dot{x}_R = A^*_{RR} \Delta x_R + B^*_R \Delta u \tag{23}$$

If taking different structural strengths under different aerodynamic loads into consideration, the model should be regarded as follows:

$$\begin{cases} \dot{x}_R = A^*_{RR|P} x_R + B^*_{R|P} \Delta U & \text{Positive loads} \\ \dot{x}_R = A^*_{RR|N} x_R + B^*_{R|N} \Delta U & \text{Negative loads} \end{cases} \tag{24}$$

As the dynamics characteristics are quite different under different conditions, the autopilot needs to be able to adapt the variation in dynamic properties by switching between two operating regions.

2.2. State Feedback Controller

As a wing's structural strength depends on the situation in terms of aerodynamic loads, for the safety and reliability of the flight performance of MWAVs, a state feedback compensator is applied to unify the closed-loop control properties of different conditions and to ensure that the vehicle always has an ideal dynamic character, as shown in Figure 5.

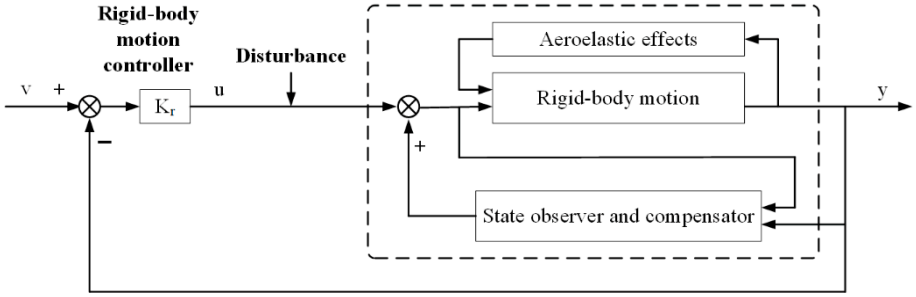


Figure 5. State observer and feedback control.

The state observer and compensator for the linearized system in Equation (23) are given as follows:

$$\begin{cases} \dot{x}_R = A^*_{RR} x_R + B^*_R (\Delta U - K\hat{x}_R) \\ \dot{\hat{x}}_R = A^*_{RR} \hat{x}_R + B^*_R (\Delta U - K\hat{x}_R) + G(y - C\hat{x}_R) \\ y = C x_R \end{cases} \tag{25}$$

where G and K are the state observer and controller matrices, respectively. If just investigating the short-period longitudinal motion [43], then $x_R = \{\alpha, q\}^T$, $\Delta U = \{\Delta_e\}^T$.

The state observer matrix G is given below in terms of T_{cII} (the transformation matrix of canonical transformations) and g_0 and g_1 (the feedback factors for pole amendments).

$$G = T_{cII}[g_0, g_1]^T = [B^*_R,\ A^*_{RR} B^*_R][g_0, g_1]^T \tag{26}$$

To obtain the desired state observer matrix G, we need to calculate the feedback factors g_0 and g_1, which were mentioned in Equation (26). Let c_1 and c_0 denote actual coefficients of the open-loop system, while $c_1{}^*$ and $c_0{}^*$ denote desired coefficients of the closed-loop system. The desired performance is specified by placing the closed-loop observer poles at a desired location, characterized by the eigenvalue λ. Based on pole placement principles, the relationship between the open-loop coefficients, desired closed-loop coefficients, and feedback factors is established, leading to Equation (27) for the closed-loop and desired closed-loop observer characteristic polynomials.

$$\begin{cases} f(\lambda) = \left|\lambda I - \left(\overline{A} - \overline{GC}\right)\right| = \lambda^2 + (c_1 + g_1)\lambda + (c_0 + g_0) \\ f(\lambda) = \lambda^2 + c_1^* \lambda + c_0^* \end{cases} \tag{27}$$

where $\overline{A}$, $\overline{C}$, and $\overline{G}$ can be expressed as follows:

$$\overline{A} = T_{cII}^{-1} A T_{cII}, \overline{C} = C T_{cII}, \overline{G} = T_{cII}^{-1} G \tag{28}$$

Then, based on different structural strengths, the desired state observer matrix G is

$$\begin{cases} G_P = T_{cII|P}\left[c_0^* - c_{0|P}, c_1^* - c_{1|P}\right] & Positive\ loads \\ G_N = T_{cII|N}\left[c_0^* - c_{0|N}, c_1^* - c_{1|N}\right] & Negative\ loads \end{cases} \tag{29}$$

As long as the eigenvalues of $(A - GC)$ have negative real parts, the estimation results of the state observer will gradually approach the measured system status. The purpose of designing state observers is to compare estimation errors and provide a clue for controller scheduling mechanism, as discussed in the following section.

Then, introduce state feedback controller into the state space equations:

$$\dot{x}_R = (A_{RR}^* - B_R^* K)x_R + B_R^* \Delta U \tag{30}$$

The adjusted transfer function is as follows:

$$\frac{\Delta\alpha(s)}{\Delta\Delta_e(s)} = \frac{b_1 s + b_0}{s^2 + (a_1 + k_1)s + (a_0 + k_0)} \tag{31}$$

The state feedback controller matrix K is given below in terms of T_{cI} (the transformation matrix of canonical transformations) and k_0 and k_1 (the feedback factors for pole amendments).

$$K = T_{cI}[k_0, k_1] \tag{32}$$

If the desired poles are designed as a_1^* and a_0^*, the state feedback gain matrix K is given as follows:

$$\begin{cases} K_P = T_{cI|P}\left[a_0^* - a_{0|P}, a_1^* - a_{1|P}\right] & Positive\ loads \\ K_N = T_{cI|N}\left[a_0^* - a_{0|N}, a_1^* - a_{1|N}\right] & Negative\ loads \end{cases} \tag{33}$$

So, by using different state observer and controller matrices, respectively, for different conditions, the properties of the vehicle closed-loop control can be maintained consistently under varying conditions by switching between different operating regions. Figure 6 shows the loop of the state feedback control configuration diagram.

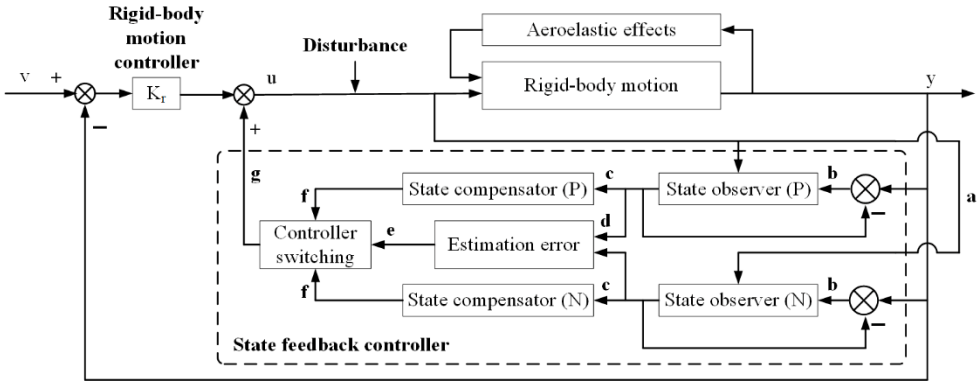


Figure 6. State feedback controller configuration.

2.3. Controller Scheduling

Due to the inconsistency of the dynamic model under different load conditions, the state feedback controller needs to switch between two corresponding operating regions. As two state observers are designed specifically for positive or negative loads, the observer with relatively smaller estimation errors represents the correct operating region for the flight control system.

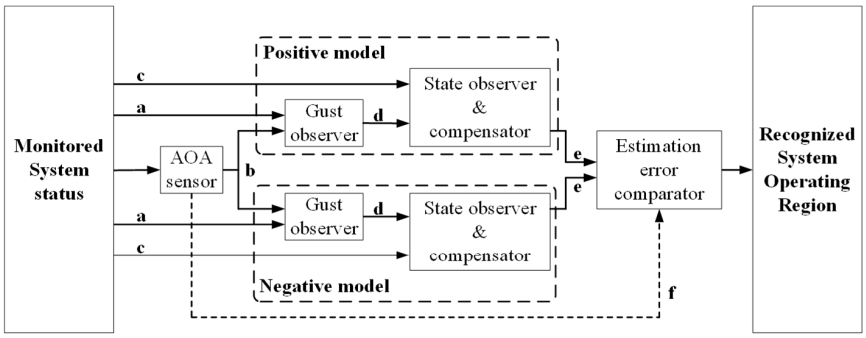
Based on Equation (25), by setting $x_R = \{\alpha, q\}^T$ and considering disturbances due to wind gusts, the state observer can be given as follows:

$$\begin{bmatrix} \dot{\alpha}_E \\ \dot{q}_E \end{bmatrix} = (A^*_{RR} - GC)\begin{bmatrix} \alpha_E \\ q_E \end{bmatrix} + (A^*_{RR} - GC)\begin{bmatrix} \alpha_M - \alpha_E \\ 0 \end{bmatrix} + B^*_R \Delta U - B^*_R K \begin{bmatrix} \alpha_E \\ q_E \end{bmatrix} + GC \begin{bmatrix} \alpha_M \\ q_M \end{bmatrix} \tag{34}$$

where α_E is defined as the estimated attack angle (e-AOA), α_M is defined as the measured attack angle (m-AOA), and the same for q. Note that here it is assumed that the MWAV is capable of sensing attack angles [44].

During actual flight of the membrane wings, there exist disturbance inputs such as gusts. Combining the theory of stochastic optimal control, we need to select control variables to achieve optimal performance indicators of the system [45]. The process of controller scheduling includes three steps, as shown in Figure 7:

1. Measure the effects of disturbances, such as attack angles in this article.
2. Estimate the response of the system based on the state observer given in Equation (34).
3. Compare the estimated and measured system states; as each model represents a specific operating region, the model with the smallest estimation error will be chosen as the recognized system operating region.



a: accelerations, angular speed, control input
b: measured angle of attack with low sampling rate
c: angular speed, control input
d: estimated unsteady angle of attack
e: estimated steady angle of attack
f: measured angle of attack, if sampling rate is high enough for error comparator

Figure 7. Recognition of system operating region.

There are two state observers, based on dynamic models of positive or negative loads, respectively. After introducing m-AOA into state observers as shown in Equation (34), they will give two e-AOAs. Comparing the estimated ones with measured ones, the state observer with the smallest errors shows the current operating region of the vehicle.

The estimation error is defined by the average error in a short period of time:

$$\begin{cases} E\left(\alpha_{E|P}\right) = \sum_{t}^{t+\Delta t} \dfrac{\left|\alpha_m - \alpha_{E|P}\right|}{|\alpha_m|} \\ E\left(\alpha_{E|N}\right) = \sum_{t}^{t+\Delta t} \dfrac{\left|\alpha_m - \alpha_{E|N}\right|}{|\alpha_m|} \end{cases} \tag{35}$$

The expected gain scheduling vector ρ is defined as follows:

$$\begin{cases} \rho = 0 & E\left(\alpha_{E|N}\right) < E\left(\alpha_{E|P}\right) \\ \rho = 1 & E\left(\alpha_{E|N}\right) \geq E\left(\alpha_{E|P}\right) \end{cases} \tag{36}$$

The gain scheduling vector is a designed signal that controls the scheduling process to switch between the control region of negative loads and positive loads. When the estimation error of the state observer based on a negative load is small, the expected gain scheduling vector ρ is 0, indicating that the system needs to switch to the control region for negative load. When the estimation error of the state observer based on the positive load is small, the expected gain scheduling vector ρ is 1, indicating that the system needs to switch to the control region for the positive load.

To ensure that control signals are continuous, a controller blending mechanism is used for the transition process. A virtual two-order closed-loop feedback system is given, with ξ representing the smoothed gain scheduling vector of controller blending during the transient process.

$$\frac{\Delta\xi(s)}{\Delta\rho(s)} = \frac{b_1 s + b_0}{s^2 + a_1 s + a_0} \tag{37}$$

By selecting suitable poles and zeros, a fast and smooth changing process can be acquired for the gain scheduling vector, and the autopilot will be quickly switched to another operating region, while the control signal remains continuous. The control signal is computed as follows:

$$\eta_X = \xi\eta_{X|P} + (1 - \xi)\eta_{X|N} (0 \leq \xi \leq 1) \tag{38}$$

3. Results

3.1. Simulation Methods

The simulation environment is designed in the time domain to involve the control system. The architecture of the simulation is similar to conventional rigid body aircraft simulation programs, and membrane wing dynamics are added to the rigid body model by switching the reference frame to a non-inertial one attached to a rigid section of the fuselage, which can be considered to be performing pure rigid body motion. The mechanics block shown in Figure 8 represents both the rigid body flight dynamics and the aeroelastic dynamics of the aircraft.

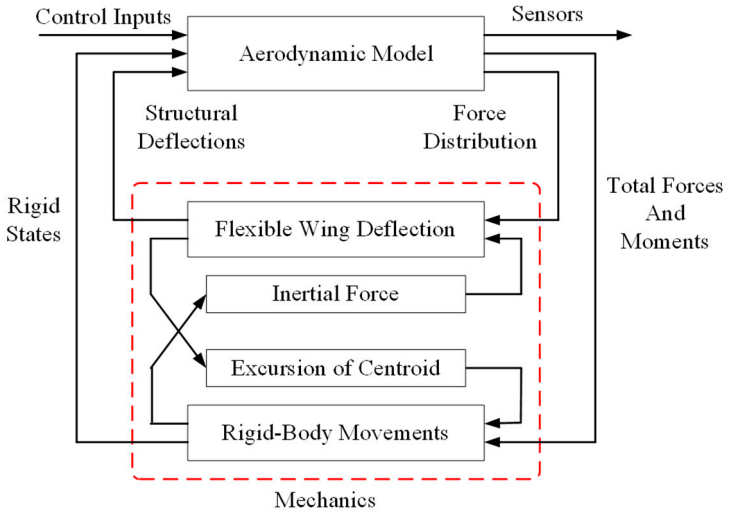


Figure 8. Flight dynamics and structural dynamics interconnection.

The rigid body dynamics are represented using the form of standard 6-DOF equations of motion, as given in Equation (39). Here, m and I_r are the aircraft mass and moments of inertia, V_r and Ω_r are the rectilinear and angular velocities defined in the body reference frame, T_g is the rotation matrix from the ground reference frame to the body reference frame for gravity, and F_r represents aerodynamics and thrust forces and moments acting on the aircraft [46].

$$\begin{bmatrix} m\left(\dot{V}_r + \Omega_r \times V_r - T_g g\right) \\ I_r \dot{\Omega}_r \times I_r \Omega_r \end{bmatrix} = F_r(t) \tag{39}$$

The membrane wing dynamics are given in Equation (40). Here, M is the mass matrix, D is the structural damping matrix, K is the stiffness matrix, and X is the elastic deformation vector. Unsteady aerodynamic forces are also included in the simulation, which is calculated based on the Theodorsen function. The Theodorsen function considers the airflow disturbances caused by wing motion and their changes over time. Its specific definition and mathematical expression can be found in [47,48].

$$\begin{cases} M\ddot{X} + D\dot{X} + KX = F\left(V_r, \Omega_r, X, \dot{X}, \ddot{X}\right) \\ X(0) = X_{N-1} \\ \dot{X}(0) = \dot{X}_{N-1} \end{cases} \tag{40}$$

In order to handle the variation in structural strength between positive and negative loads, simulation is carried out in the time domain. The coupling effects between rigid body motion and flexible deflection are calculated in turn in each cycle, as shown in Figure 9. This method makes it possible to modify the structural characteristics in each cycle. By making small changes to the structural properties in a few simulation cycles, it is possible to ensure that the transient process of the structural strength is continuous and smooth.

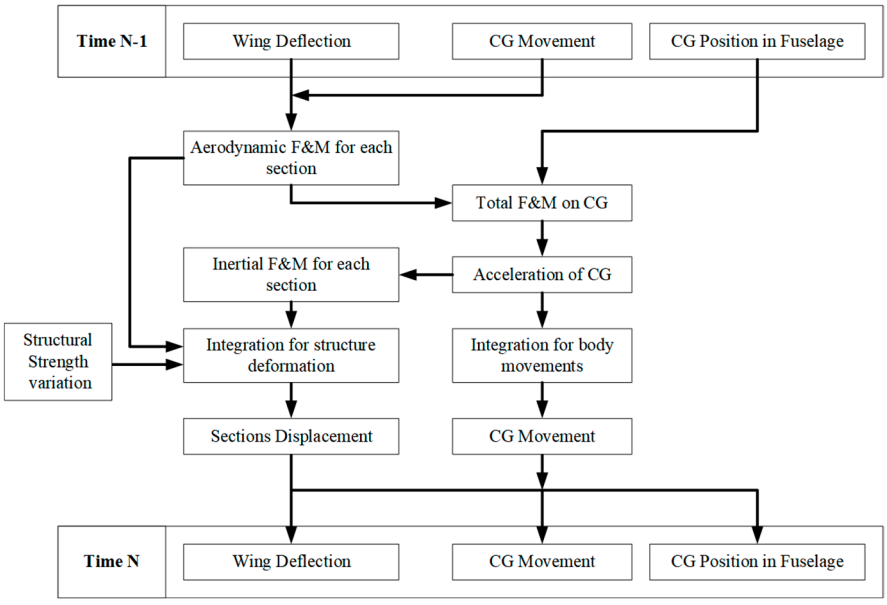


Figure 9. Simulation solution for control-based time domain aeroelastic dynamics.

The basic characteristics of the studied MWAV are presented in Table 3. The design of this platform is centered on the membrane wing, which shares many similar features with previous studies.

Table 3. Configuration properties.

Property	Value
Wingspan (m)	1.0
Length (m)	0.9
Mean aerodynamic chord (m)	0.17
Total mass (kg)	2.0
Speed (m/s)	16
Overload limit (m/s^2)	−15~20

3.2. Estimation Results of State Observer

The membrane-wing aircraft is placed under positive and negative loads separately to investigate the performance of state observers and compensators. The results are presented in Figure 10. PLSO represents the state observer under the assumption of positive attack angles, and NLSO represents the state observer under the assumption of negative attack angles.

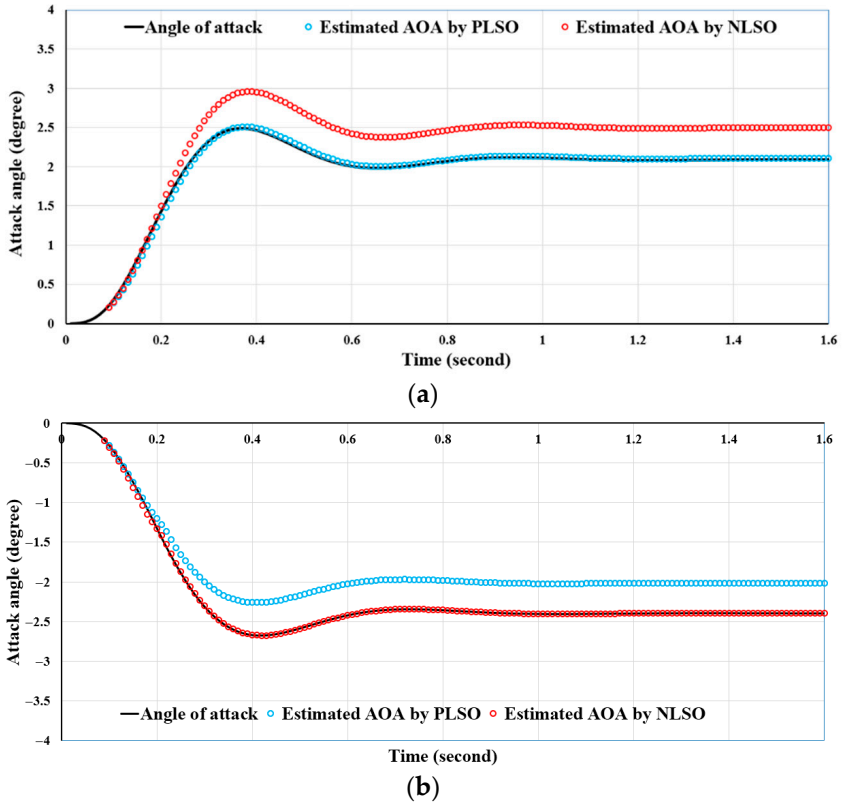


Figure 10. Estimation results of state observers: (**a**) under positive loads; (**b**) under negative loads.

Figure 10a shows that the attack angles estimated by PLSO are closer to the actual attack angles than that estimated by NLSO under positive loads; Figure 10b shows that the attack angles estimated by NLSO are closer to the actual attack angles than that estimated by PLSO under negative loads. Furthermore, we use two common quantitative metrics, the mean absolute error (MAE) and root mean square error (RMSE), to evaluate the performance of the two observers, and the results are shown in Table 4. They show that PLSO has a significantly smaller MAE and RMSE than NLSO under positive loads and vice versa. Therefore, it can be concluded that the corresponding state observer can accurately track the attack angle changes in the membrane-wing aircraft under different loads.

Table 4. MAEs and RMSEs for PLSO and NLSO.

Load Conditions	Type of State Observer	MAE	RMSE
Positive loads	PLSO	0.05	0.06
	NLSO	0.33	0.36
Negative loads	PLSO	0.31	0.34
	NLSO	0.02	0.04

The structure of the wings under negative attack angles has a weaker strength, as shown in Table 1, and a weaker structural strength leads to larger deformation. The results in Figure 10 support this analysis. It is evident that compared with the PLSO state observer, the NLSO state observer tends to give larger attack angle estimation results due to the need to compensate for the larger wing deflection. In addition, Figure 10a,b show that the absolute amplitude of the actual attack angles is higher under negative loads.

3.3. Controller Scheduling Mechanism

Based on the definition of the attack angle estimation error given in Equation (35), the average estimation error is calculated over a short period of time in the past. The purpose of this design is to prevent the value of the estimation error suffering from violent fluctuation, with the price of time latency on the variation in gain scheduling vector. This latency is particularly critical during rapid transitions between positive and negative loads, where a delayed response may cause instability or control lag. To reduce time latency, a prediction mechanism is designed, with $DevE(\alpha)$ representing the changing rate of the estimation error.

$$DevE(\alpha) = \frac{E(\alpha)_t - E(\alpha)_{t-\Delta t}}{\Delta t} \tag{41}$$

An anticipated estimation error is defined as follows:

$$\hat{E}(\alpha) = E(\alpha)_t + DevE(\alpha)\Delta t \tag{42}$$

The expected gain scheduling vector ρ is determined by the combined results of the current and anticipated estimation error.

$$\begin{cases} \rho_n = 0[E(\alpha_N) < E(\alpha_P)]AND\left[\hat{E}(\alpha_N) < \hat{E}(\alpha_P)\right] \\ \rho_n = 1[E(\alpha_N) \geq E(\alpha_P)]AND\left[\hat{E}(\alpha_N) \geq \hat{E}(\alpha_P)\right] \\ \rho_n = \rho_{n-1} - \Delta t^{-1}[E(\alpha_N) \geq E(\alpha_P)]AND\left[\hat{E}(\alpha_N) < \hat{E}(\alpha_P)\right] \\ \rho_n = \rho_{n-1} + \Delta t^{-1}[E(\alpha_N) < E(\alpha_P)]AND\left[\hat{E}(\alpha_N) \geq \hat{E}(\alpha_P)\right] \end{cases} \tag{43}$$

This approach is essential for managing rapid load reversals. When the load changes abruptly, $DevE(\alpha)$ detects the changing trend and promotes $\hat{E}(\alpha)$ predicting the future estimation error. Then, the expected gain scheduling vector ρ is determined by combining the actual estimation error at the current moment with the predicted future estimation error. Due to the introduction of the future estimation error, ρ will move towards the expected value faster than if relying solely on the actual estimation error at the current moment, enabling proactive adjustment of control parameters. We discuss four scenarios, as shown in Equation (43):

1. Scenario 1: The current NLSO has a smaller estimation error, and the future NLSO will still maintain a smaller estimation error. In this circumstance, NLSO is an advantageous observer for a short period of time, so we set ρ to stay at 0 to make NLSO work.
2. Scenario 2: The current PLSO has a smaller estimation error, and the future PLSO will still maintain a smaller estimation error. In this circumstance, PLSO is an ad-

vantageous observer for a short period of time, so we set ρ to stay at 1 to make PLSO work.

3. Scenario 3: The current PLSO has a smaller estimation error, but the future NLSO will have a smaller estimation error. In this circumstance, although PLSO currently holds an advantage, NLSO will soon become the advantageous observer. Therefore, we use $-\Delta t^{-1}$ to make ρ approach 0.
4. Scenario 4: The current NLSO has a smaller estimation error, but the future PLSO will have a smaller estimation error. In this circumstance, although NLSO currently holds an advantage, PLSO will soon become the advantageous observer. Therefore, we use $+\Delta t^{-1}$ to make ρ approach 1.

The membrane-wing aircraft is set to switch between positive and negative loads every 3 s to investigate the performance of controller scheduling. The results are shown in Figure 11.

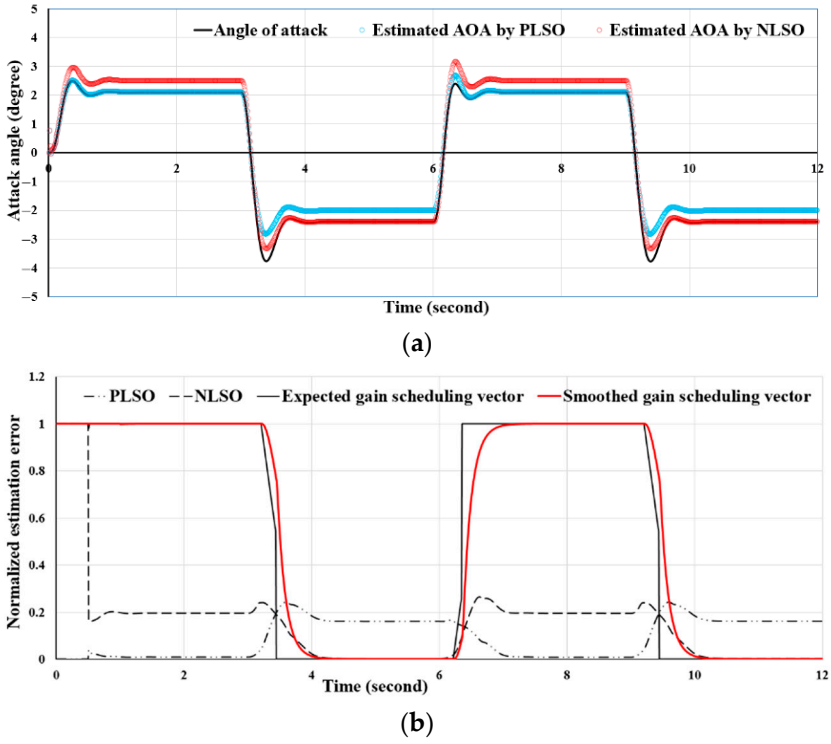


Figure 11. Controller scheduling process: (**a**) time-varying attack angle; (**b**) time-varying normalized estimation error.

From Figure 11a, we can see that PLSO can basically track the actual attack angles under positive loads and NLSO can basically track the actual attack angles under negative loads. As shown in Figure 11b, the anticipated estimation error makes the gain scheduling vector change in advance and speeds up the controller scheduling process. When the load is positive, the normalized estimation error of PLSO is smaller than that of NLSO, and vice versa. The controller will switch to the other operation region according to the normalized estimation error.

3.4. Active Gust Response Suppression

The membrane-wing aircraft is set to maintain a stable pitch angle at zero, while two continuous but opposite (1-cos)-type discrete gusts are added from 0.2 s. The velocity vector of the gusts is located in the vertical plane, perpendicular to the speed direction of the aircraft. The maximum gust speed is 5 m/s, and the duration of a single gust is 1.5 s.

The disturbance is first a positive gust, followed by a negative gust. The diagram of gusts is shown in Figure 12.

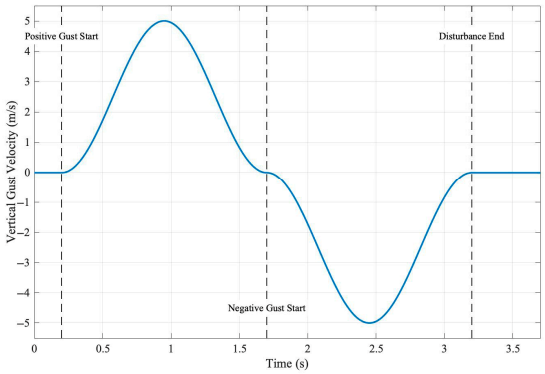


Figure 12. The diagram of gusts.

Figure 13a shows the estimated attack angles from PLSO and NLSO, comparing them with the measured attack angles.

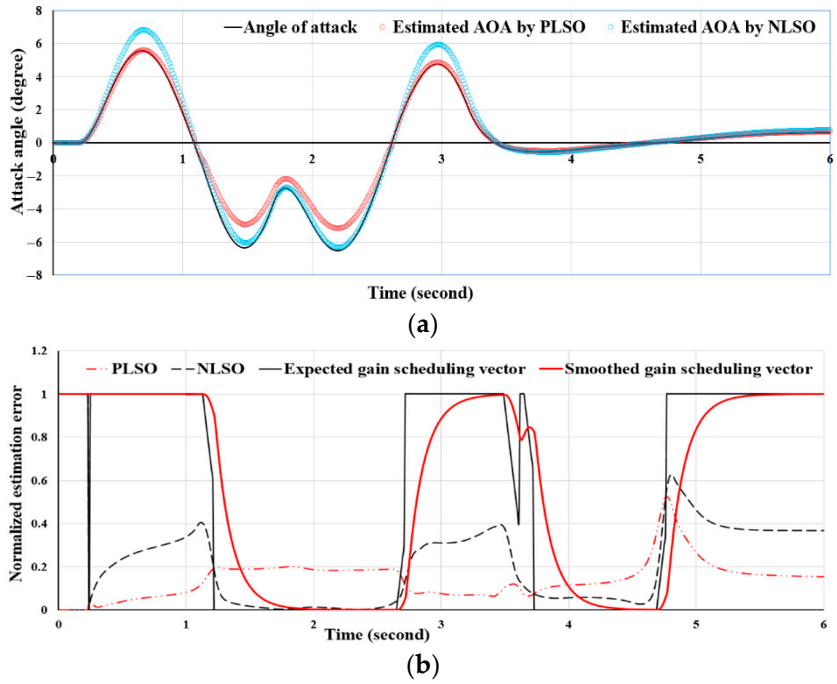


Figure 13. Controller scheduling process under a (1-cos)-type gust: (**a**) time-varying attack angle; (**b**) time-varying normalized estimation error.

From Figure 13a, it is obvious that PLSO has a much better estimation accuracy while the attack angle is positive, and vice versa. Figure 13b shows the normalized estimation error variation in the controller scheduling process, and the scheduling time reflects the variation history of attack angles: when encountering a positive load and when the attack angles are positive, the normalized estimation error of PLSO is smaller than that of NLSO, and vice versa.

A comparison of three control models is further investigated: (1) The 'Rigid control model' serves as the baseline and neglects structural deformation of the wing. The control laws derived from this model are designed assuming rigidity, making it computationally the simplest but potentially inadequate for membrane-wing aircrafts experiencing aeroelastic effects. (2) The 'Single control model' considers structural deformation of the

wing under positive attack angles. However, a key simplifying assumption is made: the model parameters under positive attack angles are assumed to remain identical under negative attack angles conditions. Control laws based on this model account for stability in the primary flight regime with positive attack angles but may suffer from inaccuracies during maneuvers involving negative attack angles because of the lack of consideration for model inconsistency under different aerodynamic loads. (3) The 'Double control model' considers the variation in structural properties that depends on different aerodynamic load conditions. Control laws derived from this model reflect scheduling control that can switch between PLSO and NLSO according to different aerodynamic loads, aiming for robust and high-performance control across the entire flight envelope, including aggressive maneuvers involving both positive and negative attack angles. This model represents the highest level of fidelity and complexity among the three. To make the three control models comparable, their longitudinal short-period motion eigenvalues are set to the same by state compensation, and they are using the same PID parameters ($k_p = -0.02$, $k_i = -0.003$) for closed-loop feedback control. Therefore, the differences between the three models are determined only by modeling errors. The three control models are simulated in the aforementioned (1-cos)-type discrete gusts environment, and the results are shown in Figure 14.

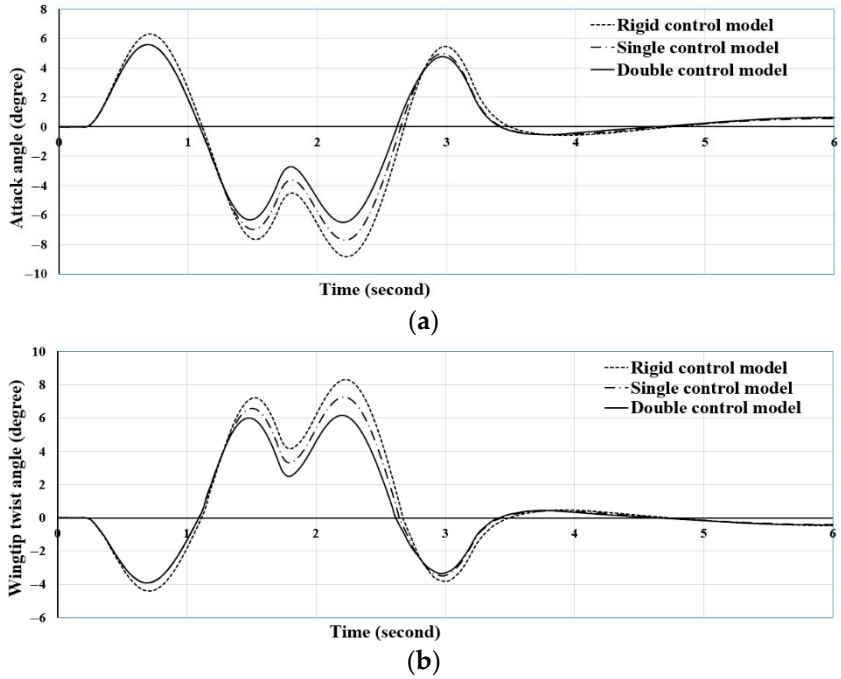


Figure 14. Control performance comparison between three different controller design schemes: (**a**) time-varying attack angle; (**b**) time-varying wingtip twist angle.

As expected, Figure 14 shows that both the attack angle and wingtip twist angle exhibit a steady-state bias under gust disturbance. The performance of the three control models is evaluated based on their deviation from the steady state: the smaller the deviation is, the stronger the model's ability to suppress gusts is. From Figure 14a, we can see that the 'Double control model' has the smallest absolute amplitude of attack angles. The absolute maximum attack angles of the 'Single control model' decreased by nearly 13% compared to that of the 'Rigid control model', and the absolute maximum attack angles of the 'Double control model' decreased by nearly 27% compared to that of the 'Rigid control model'. From Figure 14b, we can see that the 'Double control model' has the smallest absolute amplitude of wingtip twist angles. The absolute maximum wingtip twist angles of the 'Single control model' decreased by nearly 12% compared to that of the 'Rigid control model', and the

absolute maximum wingtip twist angles of the 'Double control model' decreased by nearly 25% compared to that of the 'Rigid control model'. Therefore, it can be concluded that 'Double control model' has the best performances when encountering gusts. Table 5 shows the performance comparison between the proposed scheduling control methods and other state-of-the-art gust suppression control methods.

Table 5. Performance comparison between proposed scheduling control methods and other state-of-the-art gust suppression control methods.

Gust Suppression Control Methods	Decrease in Maximum Attack Angles (Compared with Rigid Control Model)	Decrease in Maximum Wingtip Twist Angles (Compared with Rigid Control Model)
Single Control Model (Without scheduling process)	13%	12%
Double Control Model (With scheduling process)	27%	25%

In addition, it is also noticeable that when the attack angle is positive, the performances of the 'Double control model' and 'Single control model' are very similar, as during this period of time, the two controllers are working in the same operation region.

4. Discussion

In recent research, the application of micro-air vehicles has become increasingly common. Micro-air vehicles face low-Reynolds-number environments that are very unfavorable for flight. Compared with traditional fixed-wing aircrafts, membrane-wing aircrafts have better adaptability to low-Reynolds-number environments. This study combines the 6-DOF flight dynamics equations of traditional fixed-wing aircrafts and the structural dynamics equations of membrane wings to derive the dynamic equations of membrane-wing aircrafts considering aerodynamic coupling effects. On this basis, combined with the model frequency, the residual deformation of the membrane wing structure was omitted, and a simplified dynamic equation of the membrane-wing aircraft was constructed. This simplification inherently relies on two fundamental assumptions: (1) The typically low operational speeds of membrane wings underpin the adoption of a quasisteady aerodynamic assumption. Under this assumption, we neglect the time-dependent development of unsteady aerodynamic phenomena. (2) The significant mass and scale reductions result in the structural modes of membrane wings possessing natural frequencies that are substantially higher than the characteristic frequencies of the rigid-body short-period motion. This frequency separation justifies the application of linearization techniques around a nominal flight condition and allows for a lower-order model to capture the main relevant dynamics for flight control and stability analysis. The validity of these assumptions is closely tied to the specific operational envelope and scale of the membrane wings considered in this study. However, regarding scalability to larger or more complex aircrafts, some challenges arise: (1) Applying the model to substantially larger aircrafts would likely invalidate the core frequency separation assumption. Larger wings exhibit lower natural frequencies, potentially overlapping with the short-period motion and invalidating the linearized approach. Therefore, a more complex dynamic model that comprehensively considers inertial coupling and aeroelastic effects urgently needs to be constructed. (2) For configurations beyond simple membrane wings, like incorporating complex control surfaces, the quasisteady aerodynamic model may be insufficient to capture intricate flow interactions. Therefore, unsteady aerodynamic forces need to be introduced into the dynamic model.

State feedback control is used to stabilize the longitudinal motion of the aircraft. Due to the variation in wing structure strength of membrane-wing aircrafts under positive and

negative loads, PLSO observers based on positive attack angles and NLSO observers based on negative attack angles were constructed. By comparing the estimation errors of PLSO and NLSO relative to the actual attack angles, the controller is switched to a region with smaller errors to improve the effectiveness of the control.

Based on this idea, relevant simulation verification was carried out. Firstly, the membrane-wing aircraft was set to fly in pure positive-load or negative-load environments. The simulation results show that the PLSO observer of the membrane-wing aircraft can accurately estimate the attack angles under positive loads, and vice versa. On this basis, the membrane-wing aircraft was set to fly in a switching positive- and negative-load environment. The simulation results show that the PLSO observer of the membrane-wing aircraft can basically estimate the attack angles and reduce normalized estimation errors to nearly zero under positive loads, and vice versa. In addition, the introduction of anticipated estimation errors enables prediction of future flights and improves scheduling efficiency. Finally, the simulation was further extended to the gust environment that membrane-wing aircrafts may encounter during actual flight. The simulation results once again verified that the PLSO observer of membrane-wing aircraft can basically estimate the attack angles and reduce normalized estimation errors to a lower acceptable range under positive loads, and vice versa. In addition, the control performance of three controllers was compared: the 'Rigid Control Model', which considered aerodynamic coupling; the 'Single Control Model', which considered aerodynamic coupling but without considering the scheduling mechanism (controller only under PLSO observer); and the 'Double Control Model', which considered aerodynamic coupling and the scheduling mechanism. The simulation results show that the 'Double Control Model', which considers the inconsistency of positive and negative load models and scheduling mechanisms, can minimize the maximum attack angles and wingtip twist angles. Compared with the traditional 'Rigid Control Model', the absolute maximum attack angles can be reduced by nearly 27%, and the absolute maximum wingtip twist angles can be reduced by nearly 25%. This scheduling control method, which considers model inconsistency, can effectively stabilize the motion of membrane-wing aircrafts and has certain development potential.

While the simulation results are promising, translating this control strategy to real-world deployment faces several key challenges:

1. Sensor noise and estimation fidelity: The core scheduling mechanism relies on accurate real-time estimation of the attack angles. Practical attack angle sensors are subject to significant noise, bias, and dynamic errors, especially in the turbulent low-Reynolds regimes in which MWAVs operate. Noise can corrupt the error signal used for observer switching, potentially leading to inappropriate or chattering switching decisions. Quantifying the impact of specific sensor noise levels on switching logic stability and overall control performance is crucial. Mitigation strategies could involve robust filtering of the error signals to increase noise immunity.
2. Computational demands and real-time execution: The proposed architecture involves running two observers (PLSO and NLSO) in parallel alongside the main flight controller and the switching logic. This imposes a substantial computational burden. Real-time execution on typical MAV-grade embedded processors could be challenging, particularly at the high update rates required for dynamic flight control. The computational cost of the observers themselves and the switching logic need to be evaluated. Strategies to address this include optimizing the observer algorithms, exploring simplified but robust observer models for real-time use, investigating hardware acceleration, or rigorously testing the system's performance under reduced update rates.

3. Model uncertainty and environmental robustness: The simplified dynamic model, while capturing key coupling effects, inherently possesses uncertainties. Real flight involves unmodeled dynamics, parameter variations, and complex, unsteady aerodynamic effects beyond simulated gusts. The performance of both the observers and the switched controller under significant model mismatch requires further investigation. Robust control design techniques or adaptive elements might be necessary to ensure reliable operation across the operational envelope.

Despite these challenges, the demonstrated performance advantages of this scheduling strategy in simulation provide a strong motivation for overcoming them. To guide future research, several specific and promising future directions emerge:

1. Validate the proposed scheduling strategy in a realistic environment. This should involve wind tunnel testing or flight testing of a membrane-wing aircraft prototype instrumented with the necessary sensors. Key metrics to assess include robustness to unmodeled aerodynamics, structural vibrations, and real-world disturbances, directly comparing experimental results against the simulation results presented.
2. Optimize the algorithms for efficiency and rigorously evaluate the real-time performance on representative embedded platforms. Investigating simplified observer models or event-triggered updates could be valuable strategies to reduce the computational load without significant performance degradation.
3. Adopt advanced robust control methods such as H ∞ control to improve adaptability to model uncertainty and actual flight disturbances, ensuring stable flight.
4. Study strategies for active membrane-wing aircraft control, such as integrating auxiliary control surfaces or smart material actuators. This would present promising avenues for future exploration and could synergize with the developed control approach.

5. Conclusions

This paper presented an integrated dynamic model for membrane-wing aircrafts, derived from structural membrane dynamics and rigid body flight equations. To address the challenge of behavioral variations in membrane wings under different aerodynamic loads, we developed a state feedback autopilot for longitudinal attack angle control. The core innovation is a novel scheduling strategy utilizing two state observers, each designed for positive or negative attack angle flight conditions. By comparing observer estimation errors, the system identifies the current flight regime and selects the operating region yielding minimal errors, ensuring consistent control performance. Simulations under gust conditions demonstrate the effectiveness of this approach. Compared to autopilots designed for rigid aircraft, our method reduces the absolute maximum attack angle by nearly 27% and the absolute maximum wingtip twist angle by nearly 25%. This significant performance improvement confirms the autopilot's ability to maintain robust and stable flight for membrane-wing aircrafts in turbulent environments, representing a crucial advancement towards their practical autonomous operation.

Author Contributions: Conceptualization, Y.W. and Y.F.; methodology, Y.W. and Y.F.; formal analysis, Y.W., Y.F., Z.W., Y.Y. and H.L.; data curation, Y.F.; writing—original draft preparation, Y.F.; writing—review and editing, Y.W. and Y.F.; funding acquisition, Y.W. All authors have read and agreed to the published version of the manuscript.

Funding: This research received no external funding.

Data Availability Statement: Data in this work were acquired based on the simulation in Matlab R2019a, and the readers can contact us if necessary.

Acknowledgments: We are thankful for the thorough review and valuable feedback provided by the anonymous reviewers.

Conflicts of Interest: The authors declare no conflicts of interest.

References

1. Tiomkin, S.; Raveh, D.E. A review of membrane-wing aeroelasticity. *Prog. Aerosp. Sci.* **2021**, *126*, 100738. [CrossRef]
2. Deng, S.; Wang, J.; Liu, H. Experimental study of a bio-inspired flapping wing MAV by means of force and PIV measurements. *Aerosp. Sci. Technol.* **2019**, *94*, 105382. [CrossRef]
3. Bie, D.; Li, D.; Xiang, J.; Li, H.; Kan, Z.; Sun, Y. Design, aerodynamic analysis and test flight of a bat-inspired tailless flapping wing unmanned aerial vehicle. *Aerosp. Sci. Technol.* **2021**, *112*, 106557. [CrossRef]
4. Li, F.; Bai, P.; Liu, Q. Discussion about the laminar separation theory at low Reynolds numbers. *Phys. Gases* **2017**, *2*, 1–10.
5. Kay, N.J.; Richards, P.J.; Sharma, R.N. Low-Reynolds number behavior of the leading-edge suction parameter at low pitch rates. *AIAA J.* **2022**, *60*, 1721–1729. [CrossRef]
6. Guo, S.; Li, H.; Zhou, C.; Zhang, Y.; He, Y.; Wu, J. Analysis and experiment of a bio-inspired flyable micro flapping wing rotor. *Aerosp. Sci. Technol.* **2018**, *79*, 506–517. [CrossRef]
7. Chu, L.; Li, Q.; Gu, F.; Du, X.; He, Y.; Deng, Y. Design, modeling, and control of morphing aircraft: A review. *Chin. J. Aeronaut.* **2022**, *35*, 220–246. [CrossRef]
8. Wang, Z.; Sun, X.; Yang, Y.; Ge, W.; Li, D.; Bao, P.; Wu, Q.; Da, A. Design optimization and testing of a morphing leading-edge with a variable-thickness compliant skin and a closed-chain mechanism. *Chin. J. Aeronaut.* **2024**, *37*, 285–300. [CrossRef]
9. Yang, H.; Dudley, J.; Davis, J. Aeroelasticity Investigation of Generic SUAS-Membrane Wing Validation Study. In Proceedings of the 51st AIAA Aerospace Sciences Meeting including the New Horizons Forum and Aerospace Exposition, Grapevine, TX, USA, 7–10 January 2013.
10. Gehrke, A.; Richeux, J.; Uksul, E.; Mulleners, K. Aeroelastic characterisation of a bio-inspired flapping membrane wing. *Bioinspiration Biomim.* **2022**, *17*, 065004. [CrossRef]
11. Béguin, B.; Breitsamter, C. Effects of membrane pre-stress on the aerodynamic characteristics of an elasto-flexible morphing wing. *Aerosp. Sci. Technol.* **2014**, *37*, 138–150. [CrossRef]
12. Waszak, M.; Davidson, J.; Ifju, P. Simulation and flight control of an aeroelastic fixed wing micro aerial vehicle. In Proceedings of the AIAA Atmospheric Flight Mechanics Conference and Exhibit, Monterey, CA, USA, 5–8 August 2002.
13. Shyy, W.; Ifju, P.G.; Viieru, D. Membrane Wing-Based Micro Air Vehicles. *Appl. Mech. Rev.* **2005**, *58*, 283. [CrossRef]
14. Stanford, B.; Sytsma, M.; Albertani, R.; Viieru, D.; Shyy, W.; Ifju, P. Static aeroelastic model validation of membrane micro air vehicle wings. *AIAA J.* **2007**, *45*, 2828–2837. [CrossRef]
15. Xi, H.E.; Qinfeng, G.U.O.; Jinjun, W. Regularities between kinematic and aerodynamic characteristics of flexible membrane wing. *Chin. J. Aeronaut.* **2022**, *35*, 209–218. [CrossRef]
16. Li, Y.; Ge, W.; Zhou, J.; Zhang, Y.; Zhao, D.; Wang, Z.; Dong, D. Design and experiment of concentrated flexibility-based variable camber morphing wing. *Chin. J. Aeronaut.* **2022**, *35*, 455–469. [CrossRef]
17. Wang, H.; He, X.; Wang, J. Experimental study on aerodynamic and deformation characteristics of flexible membrane wing. *J. Beijing Univ. Aeronaut. Astronaut.* **2022**, *48*, 665–673.
18. Feng, S.Y.; Guo, Q.F.; Wang, J.J.; Yang, X.U. Influence of membrane wing active deformation on the aerodynamic performance of an aircraft model. *Sci. China Technol. Sci.* **2022**, *65*, 2474–2484. [CrossRef]
19. Barroso-Barderas, E.; Rodríguez-Sevillano, Á.A.; Bardera-Mora, R.; Crespo-Moreno, J.; Matías-García, J.C. Design of Non-Conventional Flight Control Systems for Bioinspired Micro Air Vehicles. *Drones* **2022**, *6*, 248. [CrossRef]
20. Negahban, M.H.; Bashir, M.; Priolet, C.; Botez, R.M. Novel Twist Morphing Aileron and Winglet Design for UAS Control and Performance. *Drones* **2024**, *8*, 392. [CrossRef]
21. Abdulrahim, M.; Garcia, H.; Lind, R. Flight characteristics of shaping the membrane wing of a micro air vehicle. *J. Aircr.* **2005**, *42*, 131–137. [CrossRef]
22. Lee, S.; Tjahjowidodo, T.; Moon, S.K. Flexible membrane wing warping using tendon-sheath mechanism. In Proceedings of the 23rd Mediterranean Conference on Control and Automation, Torremolinos, Spain, 16–19 June 2015.
23. Parancheerivilakkathil, M.S.; Pilakkadan, J.S.; Ajaj, R.M.; Amoozgar, M.; Asadi, D.; Zweiri, Y.; Friswell, M.I. A review of control strategies used for morphing aircraft applications. *Chin. J. Aeronaut.* **2024**, *37*, 436–463. [CrossRef]
24. Han, J. From PID to active disturbance rejection control. *IEEE Trans. Ind. Electron.* **2009**, *56*, 900–906. [CrossRef]
25. Guo, B.; Zhao, Z. On convergence of tracking differentiator. *Int. J. Control* **2011**, *84*, 693–701. [CrossRef]
26. Wang, Q.; Chen, Y. *Optimal Control: Theory, Method and Applications*, 1st ed.; Higher Education Press: Beijing, China, 2011; pp. 15–150.

27. Erfan, R.; Bolandi, H.; Fathi, M. Designing a fixed-time observer-based adaptive non-singular sliding mode controller for flexible spacecraft. *ISA Trans.* **2024**, *148*, 32–44.
28. Suh, P.M.; Chin, A.; Mavris, D.N. Virtual Deformation Control of the X 56A Model with Simulated Fiber Optic Sensors. In Proceedings of the AIAA Atmospheric Flight Mechanics (AFM) Conference, Boston, MA, USA, 19–22 August 2013.
29. Ryan, J.J.; Bosworth, J.T. Current and future research in active control of lightweight, flexible structures using the X-56 aircraft. In Proceedings of the 52nd Aerospace Sciences Meeting, National Harbor, MD, USA, 13–17 January 2014.
30. Hashemi, K.E.; Pak, C.; Akella, M.R. Delta adaptive flexible motion control for the X-56A aircraft. In Proceedings of the AIAA Atmospheric Flight Mechanics Conference, Kissimmee, FL, USA, 5 January 2015.
31. Buttini, T.; Moreira, F.; Silvestre, F.J.; Silva, R.G.A.d. Aeroelastic State-space Model Development Based on Frequency Response Identification and Integration with Flight Dynamics. In Proceedings of the AIAA Atmospheric Flight Mechanics Conference, Kissimmee, FL, USA, 5 January 2015.
32. Lai, K.L. Reduced-order aeroelastic modeling using coupled CFD-CSD simulations and system identification technique. In Proceedings of the AIAA/ASME/ASCE/AHS/ASC Structures, Structural Dynamics, and Materials Conference, Boston, MA, USA, 8–11 April 2013.
33. Silvestre, F.J.; Luckner, R. Experimental validation of a flight simulation model for slightly flexible aircraft. *AIAA J.* **2015**, *53*, 3620–3636. [CrossRef]
34. Zhang, L.; Ma, D.; Yang, M.; Yao, Y.; Yu, Y.; Yang, X. Experimental and numerical study on the performance of double membrane wing for long-endurance low-speed aircraft. *Appl. Sci.* **2022**, *12*, 6765. [CrossRef]
35. Yang, Y.U. Modelling and Gust Alleviation Method for Flexible Wing Biomimetic Aircraft. Ph.D. Thesis, Beijing Institute of Technology, Beijing, China, 2017.
36. Nelson Robert, C. *Flight Stability and Automatic Control*, 2nd ed.; WCB/McGraw Hill: New York, NY, USA, 1998; pp. 110–120.
37. Guo, D.; Xu, M.; Chen, S.-L.; Yao, W.-G. CFD Based Simulation of Elastic Aircraft in Maneuvering Flight. In Proceedings of the 51st AIAA Aerospace Sciences Meeting Including the New Horizons Forum and Aerospace Exposition, Grapevine, TX, USA, 7–10 January 2013.
38. Wright, J.R.; Cooper, J.E. *Introduction to Aircraft Aeroelasticity and Loads*; Shanghai Jiao Tong University Press: Shanghai, China, 2010; pp. 281–300.
39. Waszak, M.R.; Schmidt, D.K. Flight dynamics of aeroelastic vehicles. *J. Aircr.* **1988**, *25*, 563–571. [CrossRef]
40. Majeed, M.; Singh, J. Frequency and time domain recursive parameter estimation for a flexible aircraft. *IFAC Proc. Vol.* **2013**, *46*, 453–458. [CrossRef]
41. Mohamed, M.; Swaroop, S. Model simplification methods for a reduced order system of flexible aircraft. In Proceedings of the 2015 International Conference on Control, Instrumentation, Communication and Computational Technologies, Kumaracoil, India, 18–19 December 2015.
42. Looye, G. An Integrated Approach to Aircraft Modelling and Flight Control Law Design. Ph.D. Thesis, Universität Delft, Delft, The Netherlands, 2008.
43. Tregidgo, L.; Wang, Z.; Gursul, I. Unsteady fluid–structure interactions of a pitching membrane wing. *Aerosp. Sci. Technol.* **2013**, *28*, 79–90. [CrossRef]
44. Colgren, R.D. Method and System for Estimation and Correction of Angle-of-Attack and Sideslip Angle from Acceleration Measurements. U.S. Patent 6273370, 14 August 2001.
45. Astrom, K. *Introduction to Stochastic Control Theory*; Dover Publications: New York, NY, USA, 2006; p. 6.
46. Kotikalpudi, A.; Moreno, C.; Taylor, B.; Pfifer, H.; Balas, G. Low cost development of a nonlinear simulation for a flexible uninhabited air vehicle. In Proceedings of the 2014 American Control Conference, Portland, OR, USA, 4–6 June 2014.
47. Theodore, T. General Theory of Aerodynamic Instability and the Mechanism of Flutter. No. NACA-TR-496, 1 December 1979.
48. Perry, B., III. Theodorsen's and Garrick's Flutter Calculations: Revisited. *J. Aircr.* **2025**, *62*, 224–228. [CrossRef]

Disclaimer/Publisher's Note: The statements, opinions and data contained in all publications are solely those of the individual author(s) and contributor(s) and not of MDPI and/or the editor(s). MDPI and/or the editor(s) disclaim responsibility for any injury to people or property resulting from any ideas, methods, instructions or products referred to in the content.